Journal of Materials Processing Tech. 265 (2019) 191–200

Contents lists available at ScienceDirect

Journal of Materials Processing Tech.

journal homepage: www.elsevier.com/locate/jmatprotec

Effect of beam oscillation on porosity and intermetallics of electron beam welded DP600-steel to Al 5754-alloy

Soumitra Kumar Dinda[a,*], Jyotirmaya kar[a], Subhodeep Jana[b], Gour Gopal Roy[a], Prakash Srirangam[c]

[a] Department of Metallurgical and Materials Engineering, Indian Institute of Technology, Kharagpur, India
[b] Centre for Healthcare Science and Technology, Indian Institute of Engineering, Science and Technology, Shibpur, India
[c] Warwick Manufacturing Group (WMG), University of Warwick, Coventry, CV4 7AL, UK

ARTICLE INFO

Associate Editor: Prof. C.H. Caceres

Keywords:
Electron beam welding (EBW)
Beam oscillation
Al-alloy-DP-steel
Scanning electron microscopy
X-ray tomography (XCT)
Porosity
Intermetallics
Raman spectroscopy

ABSTRACT

Formation of porosity and intermetallic compounds (IMCs) were studied in electron beam welded (EBW) DP-600 steel to Al-5754 alloy joints at three different weld conditions such as without beam oscillation, with beam oscillation and with varying beam oscillation diameter. X-ray Diffraction (XRD), scanning electron microscopy (SEM), microhardness, three-dimensional X-ray computed tomography (XCT) were used to characterize porosity and IMCs distribution in these weld joints. Beam oscillation with optimum oscillation diameter (1 mm diameter) improved the weld quality by reducing the amount, maximum size and porosity contents in weld zone significantly. For IMCs, average size increased little bit but maximum size, percentage of formation and amount reduced. By increasing oscillation diameter (2 mm diameter) beyond optimum value (1 mm diameter), quality of joints was found to deteriorate with accompanying higher porosity content, average pore size, average IMCs size etc. Raman spectroscopy and gas analyzer were also used to identify and quantify the entrapped gases in the weld joint.

1. Introduction

Automotive industries have some basic agendas like reduction of vehicle exhaust emissions, improvement of occupant safety, energy saving and anti-pollution laws. Such requirements lead to the development of the materials like high strength steels, aluminium alloys, plastics and carbon fiber reinforced plastics. Owing to their lightweight and high strength, these materials decreased the weight of the cars, which in turn reduce the average fuel consumption leading to lesser CO_2 emission. According to Dharmendra et al. (2011), Joining also has a great role to play in light-weighting of components through dissimilar and tailor welded blank. Joining of steel to aluminium is a desirable option as aluminium reduce the weight of the dissimilar blank significantly. According to Potesser et al. (2006a) the primary and main issues of the steel to aluminium fusion welding are the large difference between their melting temperatures, thermal conductivities and their near to zero solid solubility between themselves that leads to the formation of brittle intermetallic compounds. Sierra et al. (2007) describes that the aluminium-rich IMCs like Fe_2Al_5, Fe_4Al_{13}, $FeAl_2$ & $FeAl_3$ are found to be more brittle compared to more iron-rich intermetallics like Fe_3Al, etc. Various welding processes have been used to join aluminium to steel like explosion welding (Kahraman et al., 2005), friction stir welding (Lee et al., 2013) conventional arc welding (Cho et al., 2014), resistance spot welding (Ambroziak and Korzeniwski, 2010), brazing (Wu et al., 2001), or laser beam welding (Wang et al., 2016), (Schweier et al., 2013). According to Suzuki and Hashimoto (1960), electron beam welding has been found to produce lowest heat input, high power density, less deformation, less contamination and less welding defects etc. with compare to all these solid state and fusion welding processes. Mohandas et al. (1999) reported that the presence of porosities, microcracks, and IMCs in electron beam welding also. Generally, these types of weld defects were characterized by conventional methods like ultrasonic, radiography, optical, SEM, EDS, etc. by Nowers et al. (2016) which are in two dimensions. Now with the aid of X-ray computed tomography (XCT), it is now possible to study different types of weld defects in three dimensions.

XCT has been used widely to study the defects and inhomogenties in various scientific research areas that include composites (Fouge, 2001), biomaterials (Jones et al., 2007), medical imaging (Bentea et al., 2015), etc. Haboudou et al. (2003) worked on a bead on plate partial penetration welding of 5083 and A356 aluminum alloys with 4kW-YAG laser welding and concluded that the dual beam welding method reduces

* Corresponding author.
E-mail address: soumitra.dinda@gmail.com (S.K. Dinda).

https://doi.org/10.1016/j.jmatprotec.2018.10.026
Received 22 June 2018; Received in revised form 9 October 2018; Accepted 21 October 2018
Available online 28 October 2018
0924-0136/ © 2018 The Author(s). Published by Elsevier B.V. This is an open access article under the CC BY license (http://creativecommons.org/licenses/BY/4.0/).

porosity formation in dissimilar joints. Nomoto et al. (2010) used microtomography to study porosity formation in CoCr alloy and Ti in similar configuration and Ti to Au-Pt alloy in the dissimilar configuration using laser welding and found the porosities ranged from 0.01% to 0.17% for both joints. Dinda et al. (2016) studied porosity formation in EB-welded Fe-7%Al alloy to steel dissimilar joints by X-ray tomography technique and quantified it for different weld parameters such as weld speed and beam oscillation. They observed that the application of beam oscillations resulted in 50% reduction in the number of porosity compared to its non-oscillating counterpart. Kar et al. (2018) studied the porosity formation in EBW Cu-SS dissimilar joints by XCT and observed that the application of beam oscillation improves the weld quality by reducing porosity formation in the joints. Milani et al. (2016) did metal inert gas (MIG) welding-brazing on automotive galvanized steel to 5754 aluminium alloy to study the effect of filler wire and wire feed speed on metallurgical and mechanical properties of these joint systems. They optimized these two parameters for controlling IMCs formation and also did failure analysis by fracture study. Cui et al. (2017) investigated on IMCs layer formation characteristics on changing of welding parameters of laser keyhole welded dissimilar 5083 alloys to Q235 low C-steel joints. They found that IMCs layer thickness decreased by increasing travel speed. Meco et al. (2014) worked on the effect of laser processing parameters such as power density and interaction time separately to understand the influence of each parameter on the formation of IMCs in the weld joint. They found that the formation of IMCs layer thickness depended on the wetting of steel substrate by molten aluminium, diffusion of aluminium and interaction time of aluminium to steel. Nguyen and Huang, (2015) worked on MIG butt-welded A5052 Al alloy to SS400 steel joints with ER4043 Al-Si filler metal. They concluded that the IMCs layer was not uniform throughout the joints and the mechanical properties like fracture toughness, tensile strength, etc. depend on the IMCs characteristics. Torkamany et al. (2010) studied the effect of pulsed laser weld parameters on IMCs formation in low carbon steel to 5754 aluminum alloy dissimilar joints. They observed that the increasing peak power, pulse duration enhances IMC formation and yields lower tensile properties. Higher welding speed was found to increase keyhole instability and crack formation. Lee and Kumai, (2006) characterized different IMCs at low C-steel to 6111 aluminium alloy laser lap joints interface. They found list of IMCs by different lab source techniques and mentioned that the average size of IMC was 500 nm towards Al-alloy region and 1 μm in central fusion region.

From above discussion, it is clear that the dissimilar joining of steel to Al invariably results in porosity and IMCs formation, which hamper the mechanical properties of the joints. Hence, it is essential to optimise the weld parameters to prevent the formation of these defects in the weld joints which needs quantified information of defects for weld conditions. In this publication, we report the characterization of porosity and IMCs formation in EB-welded DP steel to Al alloys dissimilar joints for different weld conditions. Quantification of porosity and IMCs is carried out using XCT technique.

2. Experimental details

2.1. Materials and welding procedure

DP600 steel and Al-5754 alloy plates having a thickness of 6 mm were selected as the base materials for this study. DP steel supplied by Tata Steel, Jamshedpur, India and Al-5754 Alloys by WMG, University of Warwick, UK. Table 1, given below, listed the chemical composition of both materials. Sample dimensions of 100 mm x 50 mm x 6 mm (length x Breadth x thickness) were cut from the supplied materials to do welding. The joint side face of both materials (transverse to rolling direction) was machined, polished by 600-grit emery paper. Two plates were clamped tightly for ensuring the minimum gap between them before putting it within EBW machine vacuum chamber. Before that, both samples were degreased and cleaned with acetone.

Table 1
Chemical composition of DP steel and Al alloy in weight %.

DP600 steel	C	Mn	S	P	Ni	Mo, Ti	Al	Fe
	0.085	0.91	0.008	0.015	0.017	0.001	0.04	Bal
Al-5754 alloy	Mg	Mn	Si	Zn	Cu	V	Al	Fe
	2.60	0.07	0.83	0.01	0.09	0.03	96.06	0.30

Butt welded dissimilar joints were prepared in an 80kV-12 kW EB-welding machine at Indian Institute of Technology Kharagpur, India (Dinda et al., 2016). By several trials and error attempts, beam-on-plate welding of 6 mm thick dissimilar joints was made for both oscillating beam and non-oscillating beams at the constant speed. As beam voltage (60 kV) and welding speed (750 mm/min) were maintained fixed, thus for heat requirement compensation was done by increasing beam current in a minor stage. Table 2 below shows list of weld parameters used in this present study. For every welding, an offset of 1.5 mm was used towards aluminium side from the interface. Before beam pass, preheating of steel was done at approximately 0.5 mm towards steel side. Preheating parameters were: speed 1000 mm/min, current 25 mA and voltage 60 kV.

2.2. X-ray diffraction & microscopy characterization

X-ray diffraction analysis (XRD) was carried for all weld conditions to characterize the phases present mainly in the fusion region of the joints Cu target. The diffractometer was operated in step scan mode over a 2θ range from 20° to 140° with a step size of 0.02° after smooth surface polishing and wavelength used 1.54 Å. Quantitative analysis of XRD patterns was performed by Rietveld refinement. Microstructural characterization studies were performed on the welded samples using SEM at fusion interface after final polishing without doing etching, and energy dispersive spectroscopy (EDS) point mapping was done for IMCs identification after etched the sample by Keller's reagent (2 ml HF + 3 ml HCl + 5 ml HNO_3 + 190 ml H_2O).

2.3. X-ray computed tomography (XCT)

X-ray computed tomography of weld samples was carried out using GE-phoenix®model: V/TOME/XS machine with 180 kV high power nano focus tube with sub-micron size resolution. Samples with a dimension of 1 mm x 1 mm base were cut from the full welded joints perpendicular to weld direction including both side base materials, both HAZ and fusion zone. Sub-micron range porosity distribution was calculated having minimum voxel size of approximately 3 μm and 5 μm for IMCs characterizations. Table 3 below listed the XCT parameters used for both characterizations to scan the samples.

Phoenix-Daton®(model: VG-STUDIO-MAX 2.2) software (www.volumegraphics.com, 2012) was used for analyzing the XCT data. To eliminate ring artefacts during analysis, ROI CT filtering was done for maintaining the histogram ratio between the material and background. Beam Hardening Correction (BHC) filtering was used to reduce artefacts, that may come during the scanning process. Noise reduction was done for final data to obtain clear images. 'agc' corrections were performed at the last stage of the smoothing process to solve the fixation problem if samples were tilted or shift during the scanning. In volumetric analysis tab, for porosity analysis, an automatic algorithm of the void with the threshold value of 0.1 was maintained for every analysis. In addition, for IMCs characterization, an automatic algorithm of inclusions named 'VGDefX (v2.2)' with a threshold value of 0.1 was used for every set of scan data.

Table 2
EBW process parameters used in this study.

Sample No	Beam voltage (kV)	Welding speed (mm/min)	Beam Current (mA)	Beam Oscillation		Heat input (kJ/mm) (calculated)
				Diameter (mm)	Frequency (Hz)	
Joint-1	60	750	40	Not Used	Not used	0.192
Joint-2	60	750	43	1.0	600	0.206
Joint-3	60	750	45	2.0	600	0.216

Table 3
XCT scanning parameter details used.

Parameters	Porosity /IMCs characterization
Voltage (kV)	50/ 50
Current (μA)	90/ 100
Exposure (ms)	1000/ 1000
Number of projections	1000/ 1800
Optical magnification	20X
Voxel size (μm)	2.95 / 5.18
Focal object distance (FOD)	29.03mm
Focal detector distance (FDD)	827.93mm

2.4. Raman spectroscopy & Leco gas analyzer

Raman spectroscopy analysis was carried out to determine entrapped or residual gases within the heat affected zone (HAZ) and fusion zone within the joints. With the great advancement of laser and photon detector technology, Raman spectroscopy has become a popular technique for analyzing gases present in the materials as reported by Leitch et al. (1998). For spectroscopy measurements, samples having a dimension of 4 mm diameter cylinder were cut from the full welded samples and polished it by very fine emery paper. Process parameters were the focal length of 514 nm, frequency 100 cm^{-1}, step size 0.0007 nm and grating 1800 grooves/mm. After determining the gases present within weld joints, Leco gas analyzer was used to quantify the entrapped gases in the weld joints. Three tests were performed for each sample and their average value was presented in Table 6 below.

3. Results

3.1. XRD phase analysis

Fig.1 represents XRD analysis for all three joints. The presence of different types of IMCs is observed in all three-weld joints. It is further observed that different IMCs such as FeAl, $FeAl_2$, $FeAl_3$, $FeAl_6$, Fe_2Al_5, Fe_4Al_{13} were characterized by smaller peaks and mostly overlapping with the base metal peaks. Basak et al., (2016) described the similar phenomena in case of dissimilar MIG welded AA6061-T6 to HIF steel sheet joints. Table 4 shows the quantitative information about IMCs and both base metals present. Rietveld study provides idea about different IMCs present here. It shows that total IMCs percentage value for Joint 2 (5.03%) lowest compare to other two conditioned joints.

3.2. Microscopy characterization

Fig. 2 shows SEM microscopic images of the un-etched sample showing the presence of pores for all three joint systems formed mainly in fusion zone and less number in HAZ. Fig. 3 shows the EDS point

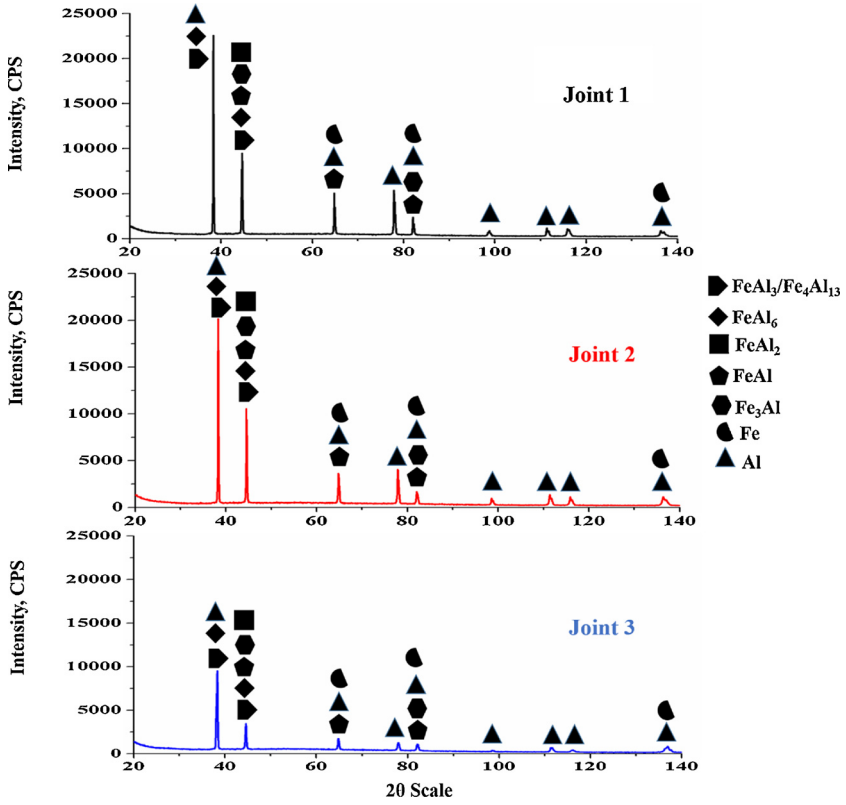

Fig. 1. XRD spectra obtained from the polished welded joints surface for all three joints.

Table 4
Rietveld analysis shows quantitative information (% value) of IMCs for all three joint systems.

Sample No	Fe (Cubic)	Al (Cubic)	Fe_3Al (Cubic)	$Fe_4Al_{13}/FeAl_3$ (Monoclinic)	FeAl (Cubic)	$FeAl_6$ (Orthorhombic)	$FeAl_2$ (Triclinic)	R_{WP}	GOF
Joint 1	10.16	81.73	0.29	1.79	0.17	4.07	1.79	6.54	1.63
Joint 2	35.28	59.69	1.40	0.33	1.82	0.25	1.23	2.92	1.33
Joint 3	18.41	68.52	1.92	3.24	0.27	5.10	2.54	4.11	1.35

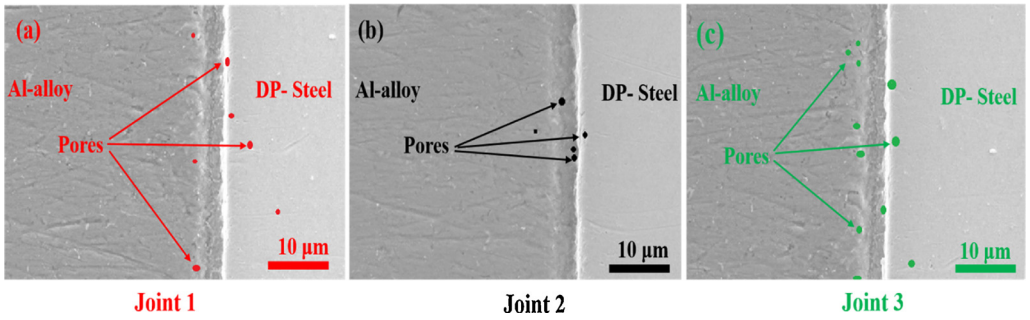

Fig. 2. SEM images showing of porosity of all three welded (a) Joint 1, (b) Joint 2 & (c) Joint 3.

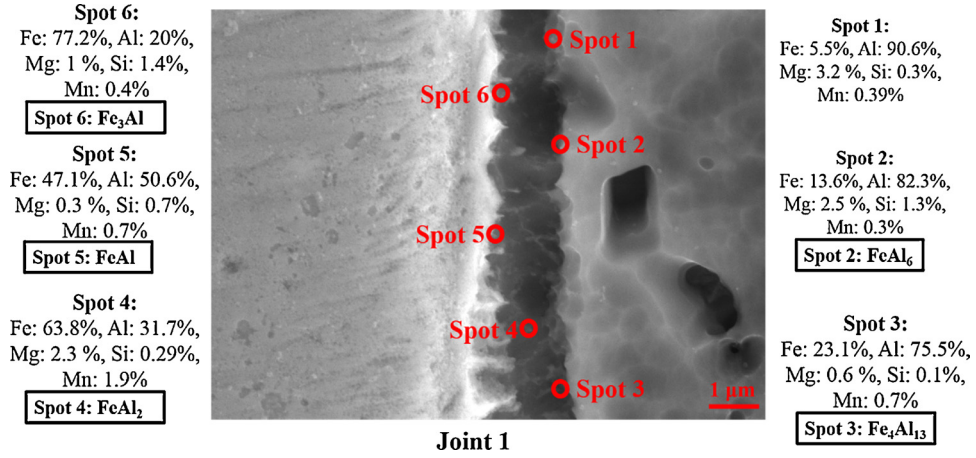

Fig. 3. SEM-EDS point mapping for Joint 1 showing different types of IMCs formed.

analysis of Joint 1 showing the presence of different types of Fe-Al intermetallic compounds with varying Fe and Al atomic percentages in their composition. Similar compounds were also observed in other two weld conditions. SEM-EDS confirms the presence of different IMCs formed at fusion zone and at fusion/ HAZ interface.

3.3. X-ray computed tomography characterization

3.3.1. Porosity study

1, Joint 2 & Joint 3 respectively. The corrugated front line represent the worn out top surface of the weld and the rear line represent the 1 mm below the top surface.

Fig. 4 shows the front view of 3-D reconstructed porosity distribution in all three EB-welded dissimilar Joints. The top portion of the image represents DP-steel, while the bottom portion represents Al alloy. For each weld condition, the volume of pores on the steel side is less compared to that on the Al-side. Fig. 5 shows the side view of pores, which strengthen our observation. It is observed that amount of pores is minimum in case of Joint 2 (weld produced by beam oscillation with optimum diameter) compared to Joint 1 (without beam oscillation) and Joint 3 (beam oscillation but with oversize oscillation diameter beyond optimum diameter). Also, for Joint 2, pores are limited only in the fusion zone compare with other two Joints where pores are scattered not only fusion zone, also in HAZ/BM (base metal) on Al side and even on steel side also in case of Joint 1.

Fig. 6 shows the individual largest pore morphologies for all three-weld conditions. Pore morphology is found to be more spherical in case of Joint 1 and irregular in shape for other two Joints. According to Jiang et al., (2011), pore morphology is characterized by using sphericity formula that is defined by Eq (1)

$$\psi = \left(\frac{36V_P^2}{A_P^3}\right)^{1/3} \quad (1)$$

Here ψ is the sphericity of pores, where ψ = 1 means a perfect sphere. Vp and Ap represent volume and surface area of the pores respectively. Fig. 7 represents the calculated sphericity values for all pore sizes. The majority of small-sized pores has sphericity approaching a value of 0.9, which indicates that the pores are near spherical in shape. For large diameter pores, the sphericity value varies between 0.3 and 0.6, which represents that the pores are irregular and non-spherical. The spherical and smooth surface of pore suggests that these pores could be formed due to dissolved or entrapped gases in the weld joint by the method of nucleation and growth. Irregular pores could be due to shrinkage during solidification of the weld joint.

From the quantified data as represented in Table 5, the average pore size in Joint 1, Joint 2 and Joint 3 are found to be 10.01 µm, 9.86 µm and 11.62 µm respectively. Given data shows that the average pore

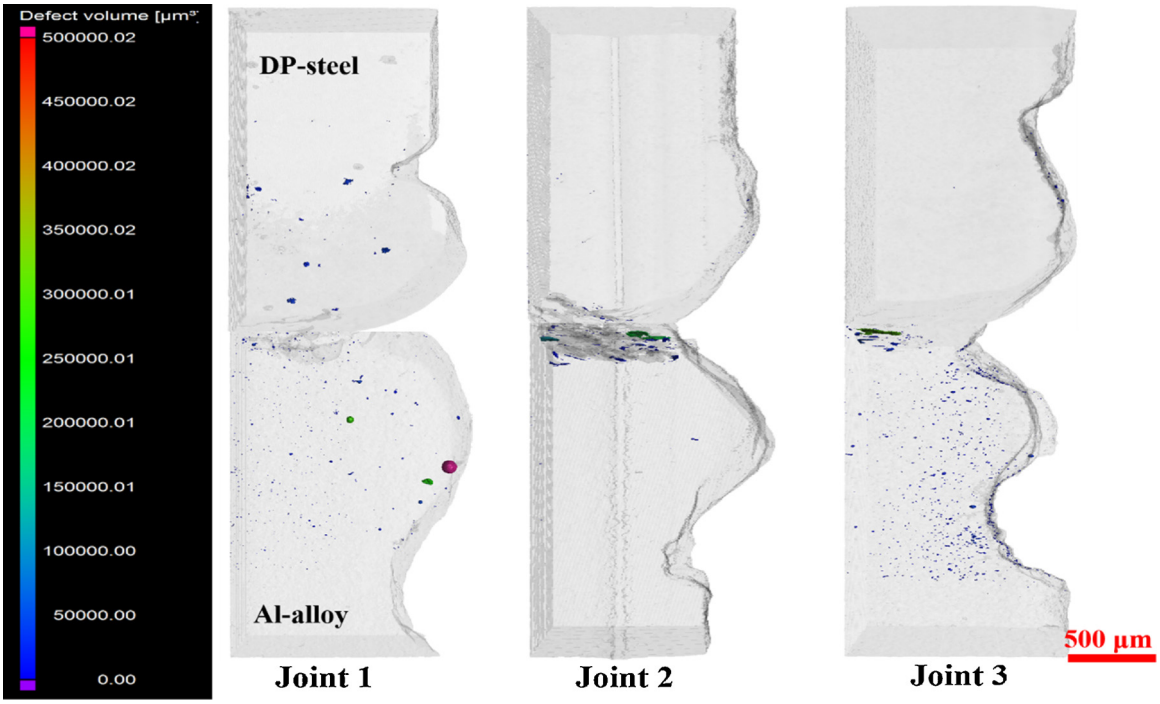

Fig. 4. Reconstructed front view 3-D transparent porosity distribution of three EB-welded Joint 1, Joint 2 & Joint 3 respectively.

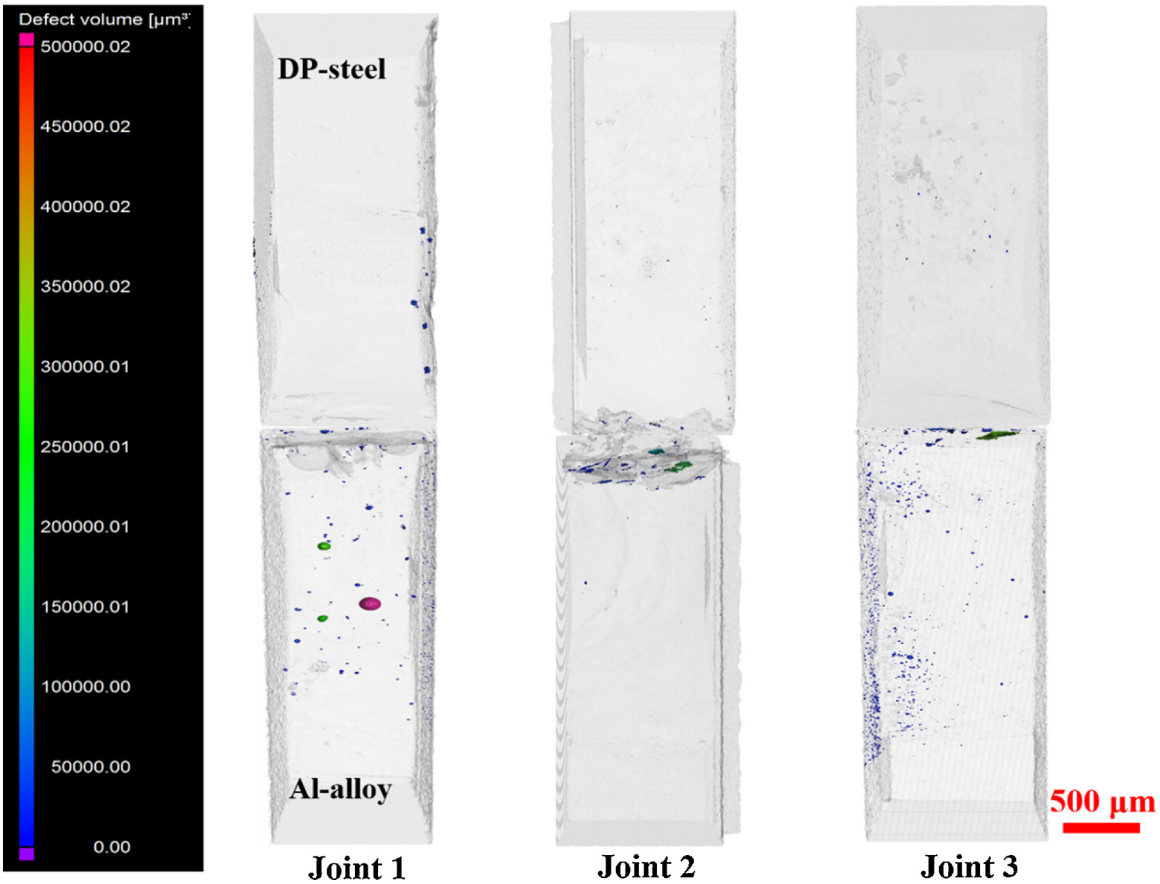

Fig. 5. Reconstructed side view 3-D transparent porosity distribution of three EB-welded Joint 1, Joint 2 & Joint 3 respectively.

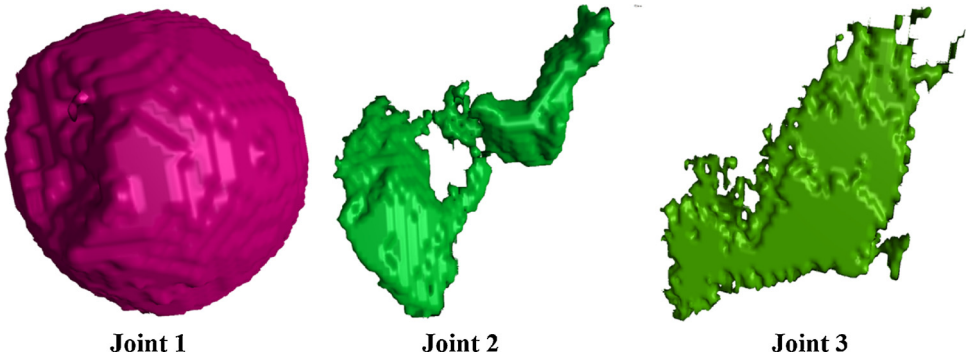

Fig. 6. Largest individual pore morphology of Joint-1 (167.4 μm), Joint-2 (253.9 μm), Joint-3 (345.3 μm).

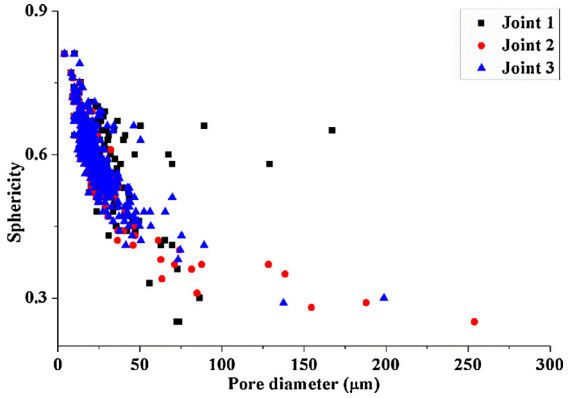

Fig. 7. shows the sphericity comparison for all three joints system.

diameter, number density are lowest for Joint 2 as compared to Joint 1. However, in case of Joint 3, all values increased as compared to other two Joints. In Joint 3, the maximum pore diameter is observed to be 345.3 μm, and number density increased to 1966 from 663 (Joint 2) and 1372 (Joint 1). Porosity percentage values of the scanned samples are lowest for Joint 2 (0.02%) compare to Joint 1 (0.05%) and Joint 3 (0.04%). Formation of larger pores having a diameter greater than 50 μm is also calculated, and it is found to be lowest for Joint 2. Quantified results are compared among all three with the help of bar chart diagram as shown in Fig. 8, and it shows the minimum presence of pores for Joint 2 and maximum for Joint 3. The magnified portion in Fig. 8 shows minimum values for Joint 2.

3.3.2. Intermetallic compounds (IMCs) study

Fig. 9 shows the front view and Fig. 10 shows the side view of 3-dimensional reconstructed IMCs distribution in EB-welded three dissimilar joint systems. The top portion of the sample represents the steel, while the bottom portion represents the Al alloy. It is found that for each weld condition, the IMCs are mostly concentrated at the steel to aluminium fusion zone interface (especially for Joint 3). IMCs are also found to spread away from a Joint interface on both sides, especially on steel side. Such spread is more prominent for Joint 1. Joint 2 shows the minimum amount of IMCs formation and Joint 3 shows the maximum and segregated at the interface. Fig. 11 shows the individual largest

Table 6
: Quantitative comparison of IMCs for three welded dissimilar joints.

Sample No	Min. Dia. (μm)	Max. Dia. (μm)	Avg. Dia. (μm)	No of IMCs	No's having > 50 μm	Avg. Dia. (μm)	% Values
Joint-1	16.32	747.3	24.02	2031	34	112.74	0.24
Joint-2	16.3	388.9	43.30	187	38	131.69	0.13
Joint-3	16.33	873.3	47.70	86	12	191.94	0.48

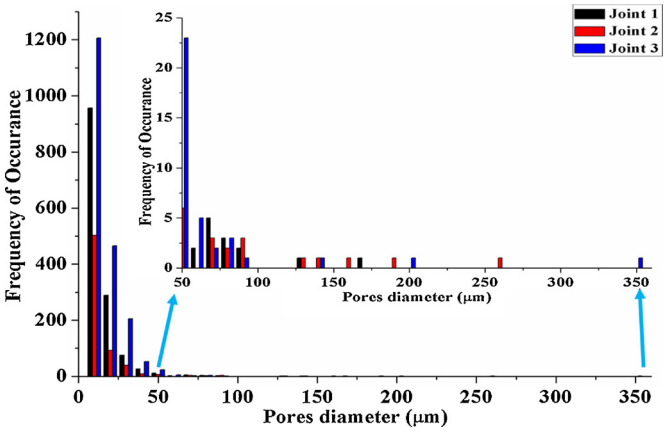

Fig. 8. shows the variation of porosity as a function of beam oscillation diameter.

compound morphologies for all three-weld conditions. Colour coding showed the size differences of formed IMCs. The blue colour showed lowest size compounds, i.e. formed for Joint 2 and red is the maximum.

Quantitative analysis is calculated and shown in Table 6. The Maximum IMC diameter is found to be 747.3 μm & 388.9 μm for Joint 1 and Joint 2 respectively and 873.9 μm for Joint 3. Calculated average diameter increased with oscillation condition compare (43.30 μm) to without oscillation condition (24.02 μm). But number density is found to be highest in Joint 1 (2031) as compared to Joint 2 (187) and minimum for Joint 3 (86). Larger size IMCs having a diameter greater than 50 μm are calculated. It shows that maximum for Joint 3 (191.94 μm) and minimum for Joint 1 (112.74 μm) and in between for

Table 5
Quantitative comparison of porosity for three welded dissimilar joints.

Sample No	Fe (Cubic)	Al (Cubic)	Fe_3Al (Cubic)	$Fe_4Al_{13}/FeAl_3$ (Monoclinic)	FeAl (Cubic)	$FeAl_6$ (Orthorhombic)	$FeAl_2$ (Triclinic)	R_{WP}	GOF
Joint 1	10.16	81.73	0.29	1.79	0.17	4.07	1.79	6.54	1.63
Joint 2	35.28	59.69	1.40	0.33	1.82	0.25	1.23	2.92	1.33
Joint 3	18.41	68.52	1.92	3.24	0.27	5.10	2.54	4.11	1.35

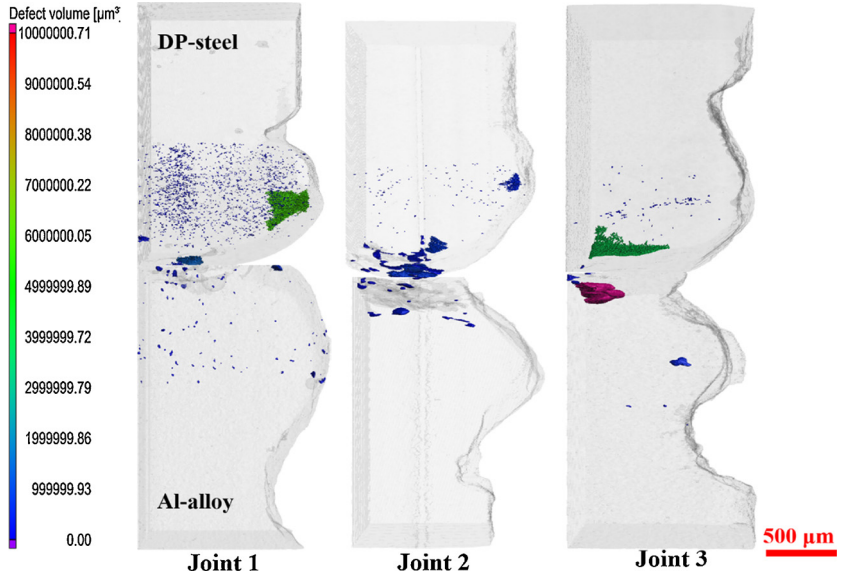

Fig. 9. Reconstructed front view 3-D transparent IMCs distribution of three EB-welded Joint 1, Joint 2 & Joint 3 respectively.

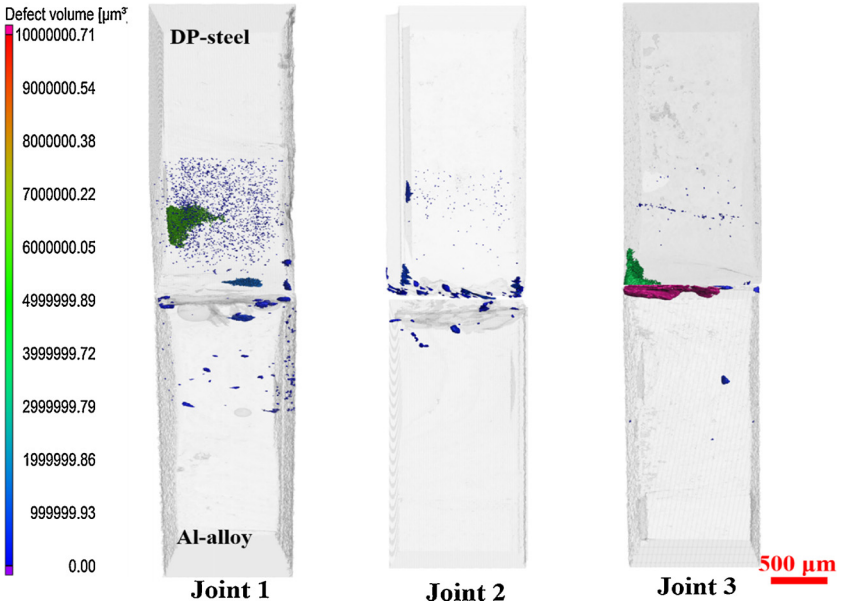

Fig. 10. Reconstructed side view 3-D transparent IMCs distribution of three EB-welded Joint 1, Joint 2 & Joint 3 respectively.

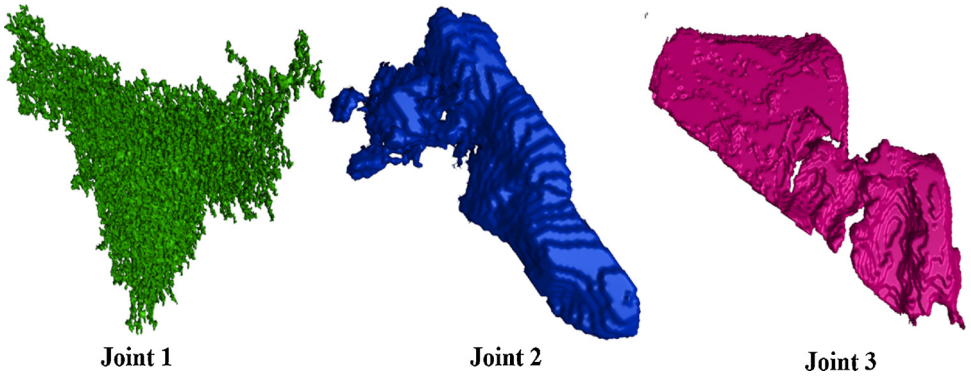

Fig. 11. Largest individual IMCs morphology of Joint-1 (747.3 μm), Joint-2 (388.9 μm) &Joint-3 (873.3 μm) respectively.

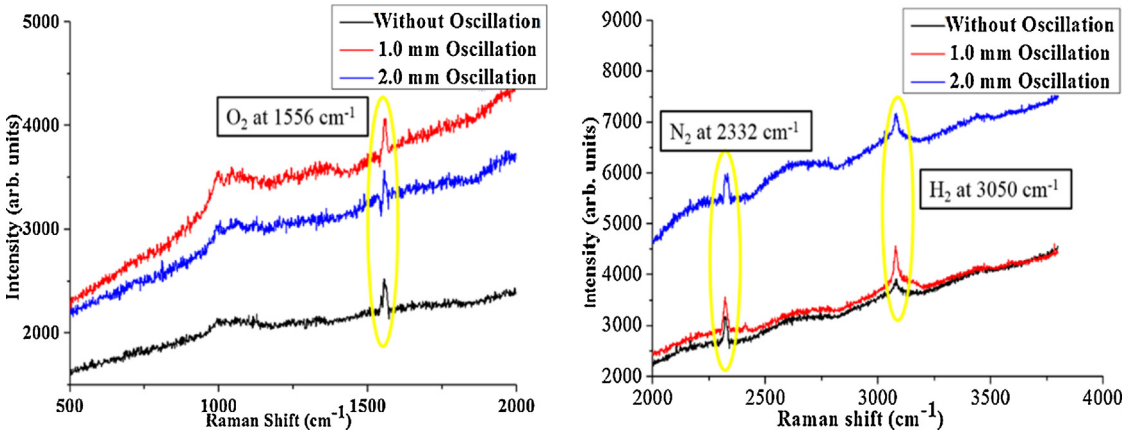

Fig. 12. Raman spectroscopy profile shows the presence of O_2, N_2& H_2 spectra for three joints.

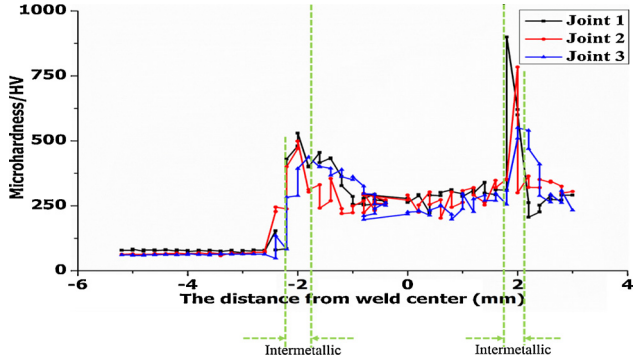

Fig. 13. Microhardness profile across the DP steel-5754 Al alloy bimetallic joints.

Table 7
Quantitative gas analysis of all three joints by H_2, N_2, O_2 Leco gas analyser.

Sample No	Condition	Radical	Results	In ppm	Total (ppm)
		O_2	0.03%	300	
Joint 1	Without beam oscillation	N_2	0.002%	20	343
		H_2	23ppm	23	
		O_2	0.01%	100	
Joint 2	With 1 mm diameter oscillation	N_2	0.005%	50	168.9
		H_2	18.9ppm	18.9	
		O_2	0.01%	100	
Joint 3	With 2 mm diameter oscillation	N_2	0.0008%	8	121.8
		H_2	13.8ppm	13.8	

Joint 2 (131.69 μm). However, the number value of larger compounds found the minimum for Joint 3. The percentage of formation of IMCs are minimum for Joint 2 (0.13%) and maximum for Joint 3 (0.48%) and in the middle for Joint 1 (0.24%).

3.4. Gas identification & quantification

Fig. 12 represents the intensity vs. Raman shift for EB-welded samples for all 3 Joints. In all three conditions, the peaks are observed at around 1550 cm^{-1}, 2331 cm^{-1}, 3050 cm^{-1} in the Raman shift representing the presence of oxygen (Buric, 2010), nitrogen (Buric, 2010) and hydrogen (Leitch et al., 1998). The source of these gases might be the entrapped gases in the faying surface or dissolved gas in the parent in the Al-alloy. After determining the type of entrapped gases in the fusion zone and HAZ of the welded joints, quantification of these gases is done by Leco H_2, N_2, and O_2 gas analyzer. From this analysis, as shown in Table 5, it is seen that for Joint 3, total gases content are 121.8 ppm that is the lowest compared to Joint 2 (169 ppm) and maximum for Joint 1 (343 ppm). Kar et al. (2018) discussed that repeated melting of the same spot during beam oscillation that allows gas to escape might be responsible for lower gas content. Besides, lowest gas content for Joint 3, might be attributed to shrinkage cavity.

3.5. Microhardness characterization

Fig. 13 represents the micro-hardness of these three EB-welded dissimilar joints across the weld bead compromising both base metal, both heat affected zone (HAZ) and weld zone. It is clear from Vickers hardness calculations that DP steel has lower hardness compare with fusion region. The average hardness of this region lies within 250 Vickers pyramid number (HV), whereas that in fusion region its increased to 290–300 HV. Aluminium alloys shows minimum hardness

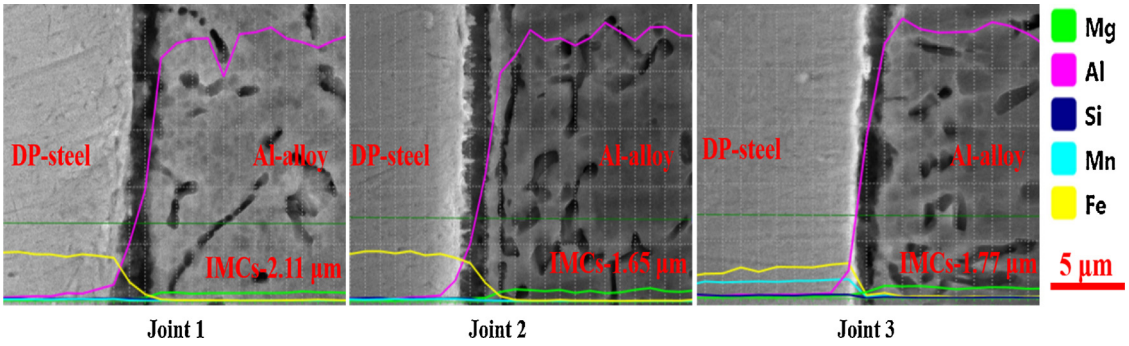

Fig. 14. Comparison of SEM-EDS line scan mapping for all three joints showing elemental variation at interface region (green line shows the path of scan) (For interpretation of the references to colour in this figure legend, the reader is referred to the web version of this article).

value of 65 HV. Note that, hardness value of both side base metals are not affected significantly at different weld conditions. Sudden increase in hardness value at the base metal-fusion zone interface on both side confirms the presence of brittle and harder intermetallic compounds. At Al- alloy side fusion zone, hardness value ranges 450–500 HV, whereas as at DP steel side lies in the range of 850–890 HV. Potesser et al. (2006b) tabulated hardness values clearly in their works of different Fe-Al IMCs as follows: FeAl (470 HV), Fe_3Al (330 HV), $FeAl_3/Fe_4Al_{13}$ (892 HV) etc. and these values are in agreement with our observation.

4. Discussion

Weld defects such that porosity and intermetallic compounds of EB-welded DP600 steel to 5754 Al alloy joints has been characterized by list of state of the art techniques. XRD and SEM showed the presence of both the defects in the weld of dissimilar joints. X-ray computed tomography was used to obtain the quantified information of weld defects. From results, it was demonstrated that porosity formation greatly depended on different welding conditions like with and without beam oscillation and oscillation diameter.

Porosity in EB-welding is likely to be formed due to either keyhole instability, or dissolved and entrapped gas at the faying surface of the weld. Huang et al. (2012) described keyhole instability phenomena and its effect on porosity formation of EB-welded titanium joints. Matsunawa (2001) recorded X-ray transmission images using high-speed photography to show keyhole phenomena. It shows that the keyhole is dynamic and this can sometimes induce porosity in welded joints. Localized solidification of the second phase in case of dissimilar welding may also form shrinkage cavities that are likely to be irregular. Kar et al. (2018) showed that localized solidification of the second phase in case of dissimilar welding may also form shrinkage cavities that are likely to be irregular. Torkamany et al. (2010) experimentally showed that the presence of sharp shrinkage leads to form cavity formation. Few researchers tried to understand the fundamental aspects of keyhole instability and found that beam oscillation could be used to control it. Blackburn et al. (2010) observed the difference by visual observation with high-speed video observation between oscillating and non-oscillating beam for keyhole observation. Schauer and Geidt (1978) predicted spiking tendency of electron beam welding process and concluded that stable keyhole leads to form spiking. Our investigation about the entrapped gases in pores, characterized by Raman spectroscopy and Leco gas analyzer (Fig. 12 & Table 7), indicated the presence of hydrogen, oxygen, nitrogen, which might come from dissolved gases (hydrogen more likely in al-alloy) in liquid or entrapped air at the faying surface.

Both porosity and IMCs were less and more uniformly distributed in case of weld prepared with beam oscillation with optimum diameter, which could be explained as follows. In case of high energy density beam at high speed like in electron beam welding, localized melting and evaporation of the material takes place just below the heat source and as soon as the heat source moves away, the said spot get solidified and the adjacent spot get melted. In this way, the joining takes place by melting and solidification of numerous tiny weld pool in succession with significant overlapping between the adjacent weld pools according to Kar et al. (2016). In case of circular beam oscillation, such overlapping of the adjacent weld pools becomes more intense because of circular oscillation path of the beam. It was reported that the Marangoni liquid convection in such tiny weld pool was quite vigorous and it pools the liquid radially outward strongly. The complicated and more intense overlapping of such tiny pools coupled with strong Marangoni convection in each pool brings in churning action leading to homogenization and more uniform distribution of defects. Besides, repeated melting of the same spot leads to escape of gases and reduce elemental segregation, super-saturation, and IMCs formation. Fig. 14 shows line scan mapping of elements for all three joints. It may be observed that Al and Fe gradient exists on the black strip at the interface indicating the IMCs thickness at the interface. It may further be observed that the amount of aluminium at the interface is maximum for Joint 3, followed by Joint 1 and it is minimum with Joint 2. If we see the iron distribution at the interface IMC layer (yellow strip), it is comparatively less steep in case of Joint 1 & 2, while it is a steep decrease in case of Joint 3. Therefore, free aluminum is expected to exist in Joint 3 and amount of intermetallic is expected to be less (because of less amount of iron at the interface) and since aluminium contained more dissolved hydrogen, more and bigger hydrogen pores are expected. Besides, the small quantity of identified gases in bigger and irregular pores in Joint 3 might be attributed to shrinkage cavity of aluminium. A minimum amount of intermetallic in Joint 2 is expected because of lesser aluminium at the interface.

5. Conclusions

In this present work, different characterization techniques were used for the characterization of weld defects such that porosity and intermetallic compounds in EB-welded full penetration butt welding of dissimilar DP600 steel to 5754 Al-Alloy joints for different welding parameters. The major outcomes of this study are as follows:

XRD and SEM analysis confirms the existence of both porosities and Fe-Al intermetallic compounds (IMCs) in the fusion zone. SEM point analysis shows elemental percentages of different intermetallic compounds. Rietveld analysis of XRD data represents the quantitative information and shows minimum percentage value at oscillation condition.

XCT result demonstrated that beam oscillation with optimum oscillation diameter (1 mm diameter) improved the weld quality by reducing the amount and size of porosity (9.86 μm & 663) compare to without oscillation condition (10.10 μm & 1372). Also by increase of oscillation diameter (2 mm) from optimum condition, quality of joints detoriates (11.62 μm & 1966).

In case of IMCs, XCT results shows that beam oscillation at optimum oscillation diameter increased the average IMCs size (43.30 μm) but decreased the number, percentage values significantly (187, 0.13%) compared to its non-oscillating counterparts (24.02 μm, 2031, 0.24%). By increasing oscillation diameter beyond optimum value, quality of joints was found to deteriorate with accompanying pore density, average pore size, average IMCs size etc. (47.70 μm, 86, 0.48%). Lager compounds formed at beam oscillation condition but numbers effectively decreased.

Presence of large amount of gases like H_2, N_2, and O_2 in the more spherical pores of Joint 1 (343 ppm, weld prepared without beam oscillation) indicated the mechanism of pore formation by nucleation and growth from dissolved and entrapped gases at the faying surface. While the lower amount of gases in bigger and more irregular pores in Joint 3 (121.8 ppm, weld prepared with beam oscillation beyond optimum oscillation diameter) indicated the formation of shrinkage porosity in the fusion zone, justified by Raman spectroscopy and Leco gas analyser.

Microhardness profile across the weld bead shows sharp increase in hardness value in both base metal side to weld region interface represents different IMCs existence.

Acknowledgements

The authors gratefully acknowledge Dr. Sourabh Chatterjee of Tata Steel, India for DP-600 steel and Prof. Richard Dashwood, Coventry University, UK for providing 5754-Al alloy sheet materials. The authors also thank Dr. Jayanta Konar of National Metallurgical Laboratory, India for gas analysis of welded joints and Central Research Facility (CRF), IIT Kharagpur for the rest of characterizations. The authors also acknowledge the financial help from the BRNS sponsored project for this work.

References

Ambroziak, A., Korzeniowski, M., 2010. Using resistance spot welding for joining aluminium elements in automotive industry. Arch. Civ. Mech. Eng. 10, 5–13.

Basak, S., Das, H., Pal, T.K., Shome, M., 2016. Characterization of intermetallics in aluminum to zinc coated interstitial free steel joining by pulsed MIG brazing for automotive application. Mater. Charact. 112, 229–237.

Bentea, E., Sconce, M.D., Churchill, M.J., Van Liefferinge, J., Sato, H., Meshul, C.K., Massie, A., 2015. MPTP-induced parkinsonism in mice alters striatal and nigral xCT expression but is unaffected by the genetic loss of xCT. Neurosci. Lett. 593, 1–6.

Blackburn, J.E., Allen, C.M., Hilton, P.A., Li, L., Hoque, M.I., Khan, A.H., 2010. Modulated Nd : YAG laser welding of Ti–6Al–4V. Sci. Technol. Weld. Join. 15, 433–439.

Buric, M.P., 2010. Gas Phase Raman Spectroscopy Using Hollow Waveguides.

Cho, D.W., Cho, W.I., Na, S.J., 2014. Modeling and simulation of arc: laser and hybrid welding process. J. Manuf. Process. 16, 26–55.

Cui, L., Chen, B., Qian, W., He, D., Chen, L., 2017. Microstructures and mechanical properties of dissimilar Al/Steel butt joints produced by autogenous laser keyhole welding. Metals (Basel) 7, 492.

Dharmendra, C., Rao, K.P., Wilden, J., Reich, S., 2011. Study on laser welding-brazing of zinc coated steel to aluminum alloy with a zinc based filler. Mater. Sci. Eng. A 528, 1497–1503.

Dinda, S.K., Warnett, J.M., Williams, M.A., Roy, G.G., Srirangam, P., 2016. 3D imaging and quantification of porosity in electron beam welded dissimilar steel to Fe-Al alloy joints by X-ray tomography. Mater. Des. 96, 224–231.

Fouge, R., 2001. Characterization by X-Ray computed tomography of decohesion. Poros. Growth Coalesc. 49, 2055–2063.

Haboudou, A., Peyre, P., Vannes, A.B., Peix, G., 2003. Reduction of porosity content generated during Nd: YAG laser welding of A356 and AA5083 aluminium alloys. Mater. Sci. Eng. A 363, 40–52.

Huang, J.L., Warnken, N., Gebelin, J.C., Strangwood, M., Reed, R.C., 2012. On the mechanism of porosity formation during welding of titanium alloys. Acta Mater. 60, 3215–3225.

Jiang, L., Chawla, N., Pacheco, M., Noveski, V., 2011. Three-dimensional (3D) microstructural characterization and quantification of reflow porosity in Sn-rich alloy/copper joints by X-ray tomography. Mater. Charact. 62, 970–975.

Jones, A.C., Arns, C.H., Sheppard, A.P., Hutmacher, D.W., Milthorpe, B.K., Knackstedt, M.A., 2007. Assessment of bone ingrowth into porous biomaterials using MICRO-CT. Biomaterials 28, 2491–2504.

Kahraman, N., Gülenç, B., Findik, F., 2005. Joining of titanium/stainless steel by explosive welding and effect on interface. J. Mater. Process. Technol. 169, 127–133.

Kar, J., Roy, S.K., Roy, G.G., 2016. Effect of beam oscillation on electron beam welding of copper with AISI-304 stainless steel. J. Mater. Process. Technol. 233, 174–185.

Kar, J., Dinda, S.K., Roy, G.G., Roy, S.K., Srirangam, P., 2018. X-ray tomography study on porosity in electron beam welded dissimilar copper–304SS joints. Vacuum 149, 200–206.

Lee, K., Kumai, S., 2006. Characterization of intermetallic compound layer formed at the weld interface of the defocused laser welded low carbon Steel/6111 aluminum alloy lap joint. Mater. Trans. 47, 1178–1185.

Lee, I.S., Kao, P.W., Chang, C.P., Ho, N.J., 2013. Formation of Al-Mo intermetallic particle-strengthened aluminum alloys by friction stir processing. Intermetallics 35, 9–14.

Leitch, A., Alex, V., Weber, J., 1998. Raman spectroscopy of hydrogen molecules in Crystalline Silicon. Phys. Rev. Lett. 81, 421–424.

Matsunawa, A., 2001. Problems and solutions in deep penetration laser welding. Sci. Technol. Weld. Join. 6, 351–354.

Meco, S., Ganguly, S., Williams, S., McPherson, N., 2014. Effect of laser processing parameters on the formation of intermetallic compounds in Fe-Al dissimilar welding. J. Mater. Eng. Perform. 23, 3361–3370.

Milani, A.M., Paidar, M., Khodabandeh, A., Nategh, S., 2016. Influence of filler wire and wire feed speed on metallurgical and mechanical properties of MIG welding brazing of automotive galvanized steel/5754 aluminum alloy in a lap joint configuration. Int. J. Adv. Manuf. Technol. 82, 1495–1506.

Mohandas, T., Banerjee, D., Kutumba Rao, V.V., 1999. Fusion zone microstructure and porosity in electron beam welds of an $\alpha+\beta$ titanium alloy. Metall. Mater. Trans. A 30, 789–798.

Nguyen, Q.M., Huang, S.C., 2015. An investigation of the microstructure of an intermetallic layer in welding aluminum alloys to steel by MIG process. Materials (Basel) 8, 8246–8254.

Nomoto, R., Takayama, Y., Tsuchida, F., Nakajima, H., 2010. Non-destructive three-dimensional evaluation of pores at different welded joints and their effects on joints strength. Dent. Mater. 26, e246–e252.

Nowers, O., Duxbury, D.J., Drinkwater, B.W., 2016. Ultrasonic array imaging through an anisotropic austenitic steel weld using an efficient ray-tracing algorithm. NDT E Int. 79, 98–108 Of, V., Computer, I., Data, V., n.d. VGStudio max 2.2.

Potesser, M., Schoeberl, T., Antrekowitsch, H., Bruckner, J., 2006a. The characterization of the intermetallic Fe-Al layer of steel-aluminum weldings. EPD Congr. 167–176.

Potesser, M., Schoeberl, T., Antrekowitsch, H., Bruckner, J., 2006b. The characterization of the intermetallic Fe-Al layer of steel-aluminum weldings. EPD Congr. 167–176.

Schauer, D., Geidt, W., 1978. Prediction of electron beam welding spiking tendency. Weld. J. 57, 189s–195s.

Schweier, M., Heins, J.F., Haubold, M.W., Zaeh, M.F., 2013. Spatter formation in laser welding with beam oscillation. Phys. Procedia. 20–30.

Sierra, G., Peyre, P., Deschaux-Beaume, F., Stuart, D., Fras, G., 2007. Steel to aluminium key-hole laser welding. Mater. Sci. Eng. A 447, 197–208.

Suzuki, H., Hashimoto, T., 1960. Electron Beam Welding. Shinku.

Torkamany, M.J., Tahamtan, S., Sabbaghzadeh, J., 2010. Dissimilar welding of carbon steel to 5754 aluminum alloy by Nd:YAG pulsed laser. Mater. Des. 31, 458–465.

Wang, P., Chen, X., Pan, Q., Madigan, B., Long, J., 2016. Laser welding dissimilar materials of aluminum to steel: an overview. Int. J. Adv. Manuf. Technol. 87, 3081–3090.

Wu, X.W., Chandel, R.S., Seow, H.P., Li, H., 2001. Wide gap brazing of stainless steel to nickel-based superalloy. J. Mater. Process. Technol. 215–221.